
HYPERSPECTRAL PIXEL UNMIXING WITH LATENT DIRICHLET VARIATIONAL AUTOENCODER

A PREPRINT

 **Kiran Mantripragada** *

Visual Computing Lab - Faculty of Science
Ontario Tech University

2000 Simcoe Street North, Oshawa, ON L1G 0C5, Canada
kiran.mantripragada@ontariotechu.net

 **Faisal Z. Qureshi**

Visual Computing Lab - Faculty of Science
Ontario Tech University

2000 Simcoe Street North, Oshawa, ON L1G 0C5, Canada
faisal.qureshi@ontariotechu.ca

March 4, 2022

ABSTRACT

Hyperspectral pixel intensities result from a mixing of reflectances from several materials. This paper develops a method of hyperspectral pixel *unmixing* that aims to recover the “pure” spectral signal of each material (hereafter referred to as *endmembers*) together with the mixing ratios (*abundances*) given the spectrum of a single pixel. The unmixing problem is particularly relevant in the case of low-resolution hyperspectral images captured in a remote sensing setting, where individual pixels can cover large regions of the scene. Under the assumptions that (1) a multivariate Normal distribution can represent the spectra of an endmember and (2) a Dirichlet distribution can encode abundances of different endmembers, we develop a Latent Dirichlet Variational Autoencoder for hyperspectral pixel unmixing. Our approach achieves state-of-the-art results on standard benchmarks and on synthetic data generated using United States Geological Survey spectral library.

Keywords Hyperspectral, Unmixing, LDVAE, Latent Dirichlet Variational Autoencoder

1 Introduction

Pixel intensity is a function of integrated reflectances from objects or materials within the instantaneous field-of-view subtended by that pixel. Therefore, a single pixel often represents a mixture of reflectances, and by extension materials. This is especially true for low-resolution Hyperspectral Images (HSI) that are captured in a remote sensing setting where each pixel may cover a large region of space Heylen et al. [2014]. The ability to identify the various materials present within a single pixel is an important problem in hyperspectral image analysis community. Within this discipline of research, this problem is often referred to as *spectral unmixing* Maggioli et al. [2018]. Spectral unmixing is often necessary to understand the composition, heterogeneity, and proportions of various materials using hyperspectral imaging, and this problem has received extensive attention within this community since its early days.

Existing approaches for pixel unmixing can be broadly classified into two groups: 1) Data-driven methods, such as Blind Source Separation models, Analysis of Principal Components (linear and non-linear), Linear Discriminant Analysis that ultimately rely upon some strategy for linear decomposition Zhang et al. [2021a], Garg et al. [2021], Khajehrayeni and Ghassemian [2021], Zhao et al. [2021], Plaza and Chang [2005]; whereas, 2) the so-called physical methods assume

* corresponding author.

access to phenomenological models of spectra that model radiance response of different materials Heylen et al. [2014], Plaza et al. [2012].

This paper develops a new method for hyperspectral pixel unmixing—identifying endmembers that constitute the pixel and estimating the mixing ratios of these endmembers. In the following discussion, we will refer to endmembers as the pure materials and as their corresponding spectral interchangeably. Furthermore, we will refer to the problem of identifying endmembers as endmember extraction, since this terminology is often used within the hyperspectral community. The proposed method casts pixel unmixing as an optimization problem within the variational inference setting. Specifically, we propose a Latent Dirichlet Variational Autoencoder whose latent representation encodes endmembers and their mixing ratios Kingma and Welling [2014]. The model assumes that endmember (spectra) can be represented using a multivariate Normal distribution, and that the endmembers and their mixing ratios can be represented as a Dirichlet distribution.

Unlike existing schemes, the proposed method does not need a endmember extraction pre-processing step. Rather our method solves endmember extraction and abundances estimation sub-problems together. Given the nature of deep learning models, our method can account for non-linearities. Additionally, our model can be used to generate spectra of mixed pixels, which is useful for generating synthetic hyperspectral data. We evaluate the proposed model on standard benchmarks—(1) synthetic data generated using United States Geological Survey spectral library (USGS) Survey et al. [2017]; (2) Cuprite cup; (3) HYDICE Urban hyd; and (4) Samson sam datasets—and show that it achieves state-of-the-art performance on commonly-used metrics.

2 Contributions

The paper develops a LDVAE (Latent Dirichlet Variational Autoencoder) for hyperspectral pixel unmixing. Unlike existing schemes, the proposed method does not need a endmember extraction pre-processing step. Rather our method solves endmember extraction and abundances estimation sub-problems together. Given the nature of deep learning models, our method can account for non-linearities. The proposed model is trained in a supervised manner (a) using (pixel spectral, abundances) pairs or (b) using (pixel spectra, abundances + endmembers). When trained using (a), the proposed model can perform “semantic labelling” of hyperspectral pixels; whereas, when trained using (b), the model can also generate spectra of mixed pixels. The ability to generate spectra for a given set of endmembers and their mixing ratios is useful when generating synthetic hyperspectral dataset for further exploration or applications to other research Zhang et al. [2021b,c, 2020], Wang et al. [2019].

We also explored the use of transfer learning, where an LDVAE trained on a suitable synthetic dataset is applied directly to the “real” dataset without further training. The assumption here is that pixel-level ground truth data is not available for the real dataset in question. We show transfer learning in action on Cuprite dataset. The synthetic dataset is generated using USGS spectral library using the dataset-level information—kind of endmembers along with their respective spectra that are present in the dataset —available for Cuprite dataset.

A secondary contribution of this work is a collection of tools that we have developed to (1) manage hyperspectral datasets, (2) parse USGS spectral library, and (3) generate synthetic hyperspectral cube using USGS spectral library. We plan to open source these tools in the future.

3 Limitations and Scope

The proposed method needs labelled data, either of the form (pixel spectra, abundances) or (pixel spectra, abundances+endmembers). Existing methods, with the exception of Borsoi et al. [2019], do not require access to labelled data. Rather these use Blind Source Separation techniques under linearity assumptions for endmember extraction and abundance estimation. A secondary limitation of our method is that it ignores spatial information. The proposed method treats each pixel individually. We aim to address this limitation in the future.

4 Related Work

Existing work on pixel unmixing in remote sensing or micro-spectroscopy belongs to one of two classes Heylen et al. [2014]: (a) physics-based methods and (b) data-driven approaches. Physics based methods seek to develop physical models for material reflectances. These methods are tedious to use given the difficulties associated with developing the aforementioned physical models. While these methods can deal with non-linearities present in the data, these methods also require highly-specialized material specific knowledge for developing the physical models, which limits their wide-spread use. Commonly used pixel unmixing methods are data driven. These attempt to identify the constituents

parts using Blind Source Separation or similar techniques. These models make linearity assumptions. Our method does not assume *a priori* knowledge of physical models for material reflectance; therefore, it belongs to the class of data driven approaches. We compare our method with a number of widely-used data-driven schemes.

Current data driven unmixing approaches comprise of two steps: (1) endmember extraction followed by (2) abundance estimation. Abundance estimation in Step 2 is sensitive to the accuracy of endmember extraction in Step 1. A commonly used method for endmember extraction is NFINER, which is an iterative algorithm that seeks to find the vertices of the n -simplex containing the pixel spectra Winter [1999]. These vertices represent endmembers. Pure Pixel Index (PPI) is another common used scheme for endmember extraction. It preprocesses the data to account for atmospheric, solar, and instrument artifacts before. The preprocessed data is transformed using dimensionality reduction analysis and noise whitening, followed by a projection onto the n -simplex hyperplane Bioucas-Dias et al. [2012], Boardman et al. [1995]. Extreme pixels, i.e., pixels closest to the vertices of the n -simplex are used to identify the endmembers. There are other schemes for endmember extraction; however, studies have found that NFINER and PPI achieve better performance than these methods Parente and Plaza [2010], Ghamisi et al. [2017], Heylen et al. [2014].

Step 2 of abundance estimation requires *a priori* knowledge of endmembers present in the pixel. Given endmembers, abundance extraction is modelled as a factorization problem in the presence of constraints, such as *sum-to-one* or *non-negative abundances* Heinz et al. [2001]. These methods often taken the form the Least Squares Projection Classifiers

$$\hat{\alpha}_{LS} = (\mathbf{E}^T \mathbf{E})^{-1} \mathbf{M}^T \mathbf{x} \quad (1)$$

where $\hat{\alpha}$ refer to abundances and where \mathbf{E} is a matrix with dimensions $D \times M$, \mathbf{x} the is the spectral signature of the pixel, D is the number of hyperspectral bands, and M is the number of materials.

Spectral-Spatial Weighted Sparse NMF (SSWNMF) is a recent method for pixel unmixing that achieves state-of-the-art performance Zhang et al. [2021a]. This method combines both spatial and spectral features for unmixing. This method also use non-negative matrix factorization that incorporates information from neighbouring pixels using a weighted-window strategy in spatial domain.

Borsio et al. Borsio et al. [2019] develop a deep learning based approach for pixel unmixing. This method explores regularization techniques to learn latent representations that are amenable to vertex component analysis for endmember extraction. The extracted endmembers are subsequently used to train deep learning model to reconstruct pure pixels. Our approach differs in that we force the latent representation to be a Dirichlet distribution that directly represents endmembers and their mixing ratios (abundances).

In conclusion, linear techniques underlie the most commonly used schemes for endmember extraction and abundance estimation. We compare the proposed LDVAE against seven commonly used techniques for pixel unmixing techniques. SSWNMF method achieves state-of-the-art results, and we follow the evaluation scheme, including both datasets and metrics, presented in Zhang et al. [2021a] to compare our method against seven other schemes.

5 Method

The problem of pixel unmixing can be understood in terms of topic modeling as explored in Blei’s work on Latent Dirichlet Allocation Blei et al. [2003], in which a set of topics might generate a document. The goal of LDA is to (1) discover these topics and (2) estimate to what degree each topic contributes to a document. In this work, we treat each (hyperspectral) pixel as a document and each endmember (i.e., pure material) as a topic. Our assumption is that these endmembers are mixed together to generate the pixel (i.e., the observed spectra). Endmembers, along with their abundances are akin to the distribution of topics in a document; therefore, we can represent endmembers (which topic) and abundances (how much) as Dirichlet Distribution given its n -simplex.

We cast the problem of unmixing as one of constructing a latent representation that follows a Dirichlet Distribution. We also seek a method that constructs a spectra given a set of endmembers and their mixing ratios. It turns out that both these tasks can be accomplished using a Latent Dirichlet Variational Autoencoder, which we discuss next.

5.1 Latent Dirichlet Variational Autoencoder (LDVAE)

Our model uses the VAE architecture shown in Figure 1; however, in our setting, the model is set to learn the parameters α of a Dirichlet Distribution in the latent space \mathbf{z} .

The abundances \mathbf{z} are sampled from the distribution and fed into the decoder. The decoder reconstructs the spectral signal $\hat{\mathbf{x}}$ given the latent vector \mathbf{z} . Here \mathbf{x} represents the input spectra and \mathbf{z} is a sample from the Dirichlet Distribution in the n-simplex form.

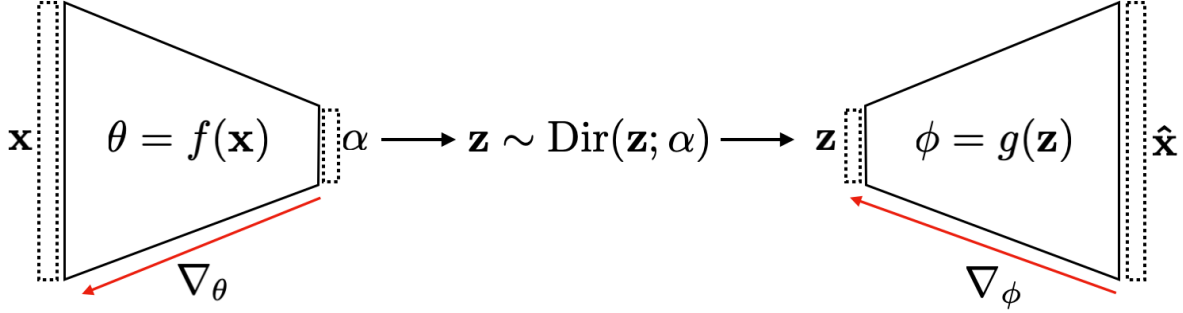


Figure 1: Latent Dirichlet Variational Autoencoder.

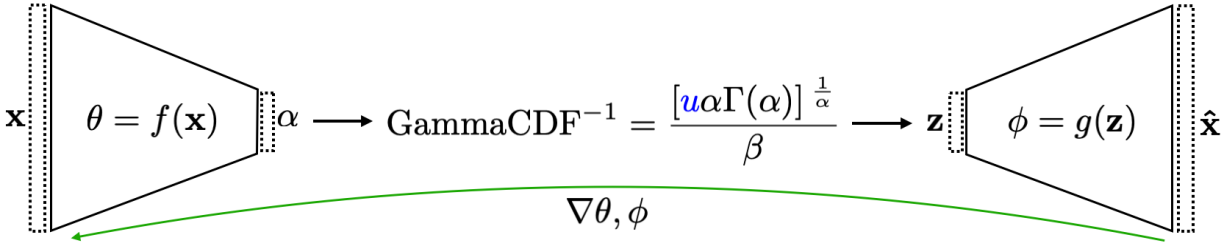


Figure 2: Inverse Gamma CDF as a replacement for the sampler function of a Dirichlet PDF.

5.1.1 Dirichlet as a multivariate Gamma Distribution

As described in Section 5.1, we need to sample \mathbf{z} from a probability distribution so we can run the forward pass during training and inference. However, the sampling function is not differentiable, which prevents the backpropagation of the gradients ∇_θ and ∇_ϕ from the decoder stage to the encoder (see Figure 1). Therefore, we need to use a reparameterization trick, similar to the one used by Kingma *et al* let@tokeneonedotfr for multivariate Normal distributions Kingma and Welling [2014]. Specifically, we follow the method proposed in Joo *et al.* [2020] and reparametrize the Dirichlet Distribution as follows

$$\mathbf{z} = \text{GammaCDF}^{-1}(u, \alpha, \beta) = \frac{[u\alpha\Gamma(\alpha)]^{\frac{1}{\alpha}}}{\beta} \quad (2)$$

The Dirichlet PDF can be represented by a multivariate Gamma Distribution, and we use the Inverse Gamma Cumulative Density Function (Equation 2) to generate the values of \mathbf{z} . In Equation 2, $\Gamma(\cdot)$ is the Gamma function, α is the concentration parameter, β is a normalization factor to make sure the vector \mathbf{z} is in the n-simplex form, and u is the parameter responsible for the randomness of $\hat{\mathbf{x}}$.

5.2 Spectral Reconstruction with Multivariate Normal Distribution

The reconstruction of the input features $\hat{\mathbf{x}}$ is a necessary step for three reasons: 1) to make sure the encoder is generating a proper (reduced) representation of the input \mathbf{x} ; 2) the decoder must be able to generate the spectral signal for any combination of abundances not seen during training; and 3) so the model is also capable of extracting endmembers², which is explained in the Section 7.

$$\begin{aligned} \mathbf{x} &\sim \text{Normal}(\mathbf{x}; \mu, \Sigma) \\ \mathbf{x} &= \{x_1, x_2, x_3, \dots, x_k\} \\ \mu &= \{\mu_1, \mu_2, \mu_3, \dots, \mu_k\} \\ \sigma &= \text{diag}(\sigma_1, \sigma_2, \sigma_3, \dots, \sigma_k) \end{aligned} \quad (3)$$

²The decoder technically “generates” endmembers, but we use “endmember extraction” to be in accordance with the common terminology in the field of spectroscopy and remote sensing.

5.3 ELBO Loss Function

In order to find the approximate Dirichlet PDF, we minimize the divergence between the two PDFs (ground truth vs. estimated). The Kullback-Leibler (KL) divergence is commonly used in machine learning for this task, however, due to an intractability of $p(\mathbf{x})$, we need to isolate this term, which gives us the Evidence Lower Bound (ELBO) function:

$$\mathcal{L}(\mathbf{x}; \theta, \phi) = \mathbb{E}_{q_\theta} [\log p_\phi(\mathbf{x}|\mathbf{z})] - KL(q_\theta(\mathbf{z}|\mathbf{x})\|p(\mathbf{z})) \quad (4)$$

For more details on the derivation of the ELBO function, please see Pinheiro Cinelli et al. [2021], Blei et al. [2017], Kingma and Welling [2014], Fox and Roberts [2012]. The second term on the right-hand side of Equation 4 is another KL-divergence term, which is tractable and encompasses the approximation between the prior and the estimated Dirichlet PDFs. The next step is to rewrite the KL term on the Equation 4 for Dirichlet Distributions according to the demonstration presented in Joo et al. [2020]:

$$\begin{aligned} KL[q(\mathbf{z}, \mathbf{x}; \hat{\alpha})\|p(\mathbf{z}; \alpha)] &= \sum \log \Gamma(\alpha_k) - \sum \log \Gamma(\hat{\alpha}_k) \\ &+ \sum (\hat{\alpha}_k - \alpha_k) \frac{d}{dx} \ln \Gamma(\hat{\alpha}_k) \end{aligned} \quad (5)$$

where $\Gamma(\cdot)$ is the Gamma function, α is the concentration parameter of the Dirichlet prior, and $\hat{\alpha}$ is concentration parameter of the estimated Dirichlet.

The first term of the right-hand side of equation 4 makes sure that the model also learns to reconstruct the spectral signal $\hat{\mathbf{x}}$, allowing it to generate spectra of endmembers and also of mixed pixels.

6 Experiments and partial results

We separated our experiments following the same criteria used by Zhang et al. in Zhang et al. [2021a]. First, we evaluate the capability of endmembers extraction using the SAD (Spectral Angle Distance) metric. Secondly, we evaluate the classification errors, i.e., the model's capability to estimate the abundances from each pixel.

The evaluation of reconstruction and endmember extraction are measured using the RMSE (Root Means Square Error) metric. Both evaluation metrics are described below. A comprehensive description of the various distance metrics, including SAD and RMSE can be found in Deborah et al. [2015], Zhu [2017], Borsoi et al. [2019]. In this section, we describe the set of experiments and we present the results of signal reconstruction capability. Despite not being the main task of the model, the reconstruction is an important step towards the extraction of endmembers.

6.1 Spectral Angle Distance (SAD)

The Spectral Angle between two hyperspectral signals can be computed as:

$$SAD_i = \arccos \left(\frac{\mathbf{x}_{e,i}^T \hat{\mathbf{x}}_{e,i}}{\|\mathbf{x}_{e,i}^T\| \|\hat{\mathbf{x}}_{e,i}\|} \right) \quad (6)$$

where \mathbf{x}_e is the HSI spectra of the endmember generated by the decoder of LDVAE, $\hat{\mathbf{x}}_e$ is the HSI spectra of the reference endmember, for each material i . This distance metric can demonstrate the accuracy of endmembers extraction. In our experiments, we compute the SAD for each material present in the dataset. Notice that \mathbf{x}_e has the same dimensionality of the regular pixels \mathbf{x} , however it represents a pixel of a pure material.

6.2 Root Means Square Error (RMSE)

We use the RMSE metric to evaluate the classification results. We compare the distance of the two vectors of abundances: predicted and ground truth. We compute the RMSE for each material present in the image. Therefore, we can evaluate the capability of the model to predict the abundances vector, which is the multinomial classification of each pixel.

$$RMSE_i = \sqrt{\frac{1}{N} \sum_1^N (\mathbf{z}_{i,n} - \hat{\mathbf{z}}_{i,n})^2} \quad (7)$$

where $\hat{\mathbf{z}}_i$ is the estimated vector of abundances in the latent space of the LDVAE, \mathbf{z}_i is the abundances vector from ground truth, and N is the number of samples evaluated, for each material i .

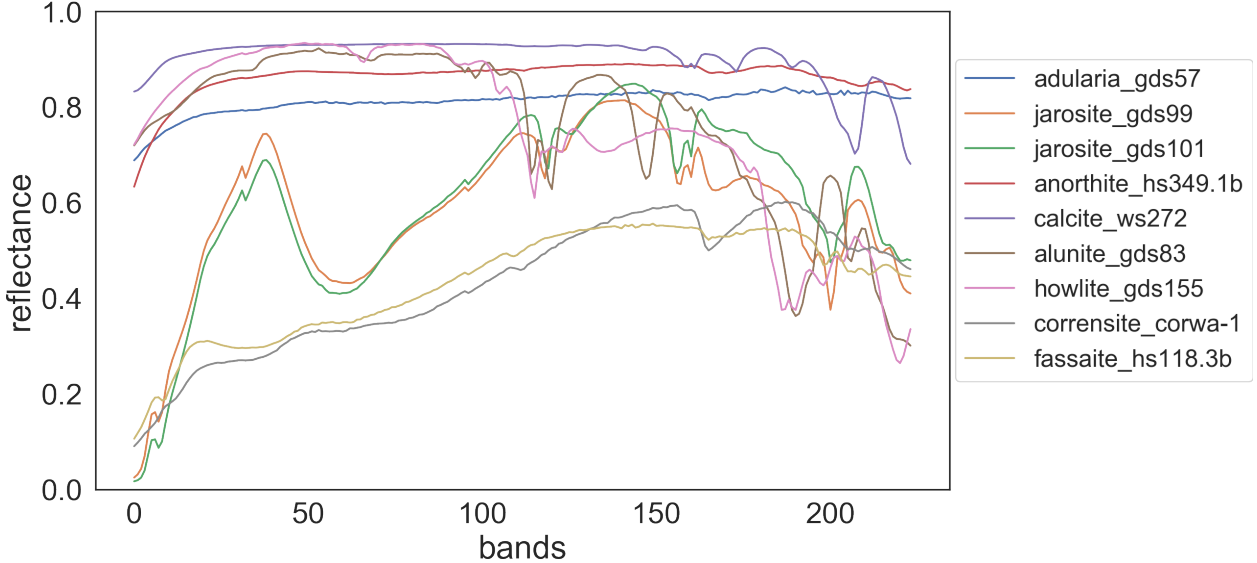


Figure 3: Synthetic HSI: Spectral signature of the endmembers from USGS Library Survey et al. [2017].

6.3 Means Square Error (MSE)

We also evaluated the capability of the model to reconstruct pixels as follows:

$$MSE = \frac{1}{N} \sum_1^N \frac{1}{D} \sum_1^D (\mathbf{x}_{d,n} - \hat{\mathbf{x}}_{d,n})^2 \quad (8)$$

where $\mathbf{x}_{d,n}$ is the n -th pixel reconstructed by LDVAE with dimension D , $\hat{\mathbf{x}}_{d,n}$ is reference n -th pixel from ground truth, N is the number of samples evaluated, and D is the number of bands. The MSE metric is an indication of the quality of the reduced representation (\mathbf{z}), and it is intrinsically represented by the first term of the loss function (equation 4) as the expected value of $\log p(\mathbf{x})$ when $p(\mathbf{x})$ takes the exponential form (as in the MVN distributions). More information can be found in Kingma and Welling [2014].

6.4 Synthetic Data

We generated two synthetic HSI datasets using the United States Geological Survey (USGS) spectral library Survey et al. [2017]. Each image contains 128x128 pixels, 224 spectral bands, and 9 classes: Adularia GDS57, Jarosite GDS99, Jarosite GDS101, Anorthite HS349.1B, Calcite WS272, Alunite GDS83, Howlite GDS155, Corrensite CorWa-1, and Fassaite HS118.3B. This list of endmembers was selected in order to match the datasets used in Zhang et al. [2021a], Li et al. [2021], thus allowing comparable metrics. The first dataset was used for training and validation. The second dataset was used for model evaluation.

6.5 Cuprite Dataset

The Cuprite HSI dataset covers a region around Las Vegas, NV, US. This image, with dimensions 512x614 contains 188 spectral channels and there are 12 minerals present in the scene: Alunite, Andradite, Buddingtonite, Dumortierite, Kaolinite1, Kaolinite2, Muscovite, Montmorillonite, Nontronite, Pyrope, Sphene, and Chalcedony. Since there is no ground truth of abundances for this dataset, we generated a synthetic image using the same materials, to train our model. Then we tested with the real Cuprite data.

6.6 Urban (HYDICE) Dataset

The HYDICE Urban dataset hyd is widely used in the studies of HSI pixel unmixing. The image contains 307x307 pixels, each of which corresponds to a $2 \times 2 \text{ m}^2$ area, and 162 channels. In this study we used the version with 6 endmembers: Asphalt, Road, Grass, Tree, Roof, Metal, Dirt. However there are other versions with 4 and 5 endmembers also available. For more information on the HYDICE Urban dataset, refer to the work of Zhang et al. in Zhang et al. [2021a]. We split this dataset into training and evaluation using a 50/50 strategy.

Table 1: Statistics of reconstruction errors (MSE and SAD)

	SAD	synthetic MSE	SAD	cuprite MSE	SAD	hydice_urban MSE	SAD	samson MSE
mean	0.0360	0.0033	0.0903	0.0121	0.0830	0.0010	0.1236	0.0108
std	0.0589	0.0024	0.0363	0.0035	0.0787	0.0004	0.1359	0.0043
min	0.0012	0.0007	0.0364	0.0031	0.0144	0.0004	0.0108	0.0002
max	0.2846	0.0106	0.2652	0.0186	1.0243	0.0018	1.0124	0.0180

Table 2: SAD results for Synthetic Data (The results of the other algorithms are collected from Zhang et al. [2021a]).

	LDVAE	SSWNMF	SGSNMF
SNR=20dB	0.0079 ±0.01	0.0636 ±0.40	0.0782 ±0.50
SNR=30dB	0.0034 ±0.00	0.0122 ±0.01	0.0176 ±0.03
SNR=40dB	0.0080 ±0.01	0.0029 ±0.02	0.0033 ±0.03
SNR=50dB	0.0023 ±0.00	0.0012 ±0.02	0.0019 ±0.02
no noise	0.0086 ±0.01	-	-

6.7 Samson Dataset

The Samson dataset sam is a small image with (95x95) pixels and 156 channels. This data is not degraded by the blank channels or channels with high noise; therefore. There are three targets in this image: Soil, Tree and Water. We isolated the samples for training and evaluation using a 80/20 split, so to prioritize training over tests looking for better model performance.

6.8 Signal Reconstruction

We also evaluated the performance of signal reconstruction of the LDVAE model. Despite not being the main task, these metrics are good indicators of how the model can generate the spectra of pure materials and to generate new pixels. The performance of signal reconstruction is presented in the table 1. We show the results of the two distance metrics to evaluate the capability of the model to generate \hat{x} given an arbitrary vector of abundances. Both metrics demonstrate LDVAE can generate new pixels that closely match the original pixels.

7 Results and Discussion

Usually, unmixing algorithms solve one of the two following tasks: 1) endmember extraction, i.e., separating the spectra of pure materials from the mixed pixel, and 2) estimation of abundances, assuming the mixed pixel is a linear combination of the endmembers. The standard methods require the computation of endmembers *a priori*, and after that, the endmembers are used to compute the abundance maps.

Conversely, our method can calculate the abundances using only the spectra of a single pixel (Figure 4). The LDVAE model can also generate the spectra of endmembers from the abundances vector with the one-hot representation of classes, passed into the decoder (Figure 5). As opposed to the previous methods, the neural network architecture can also learn non-linearities in the composition of mixed pixels, therefore, arguably, capable of learning a “function” that can estimate the abundances and generate endmembers more accurately. The non-linearities are usually more present in

Table 3: RMSE results for Synthetic Data (the results of the other algorithms are collected from Zhang et al. [2021a]).

	LDVAE	SSWNMF	SGSNMF
SNR=20dB	0.0050 ±0.00	0.1339 ±0.20	0.1322 ±0.40
SNR=30dB	0.0357 ±0.01	0.0386 ±0.20	0.0391 ±0.30
SNR=40dB	0.0358 ±0.01	0.0122 ±0.03	0.0148 ±0.05
SNR=50dB	0.0359 ±0.01	0.0041 ±0.02	0.0059 ±0.05
no noise	0.0050 ±0.00	-	-

Table 4: SAD results for Cuprite Dataset (The results of the other algorithms are collected from Zhang et al. [2021a]).

	LDVAE	SSWNMF	SGSNMF	VCA
Alunite	0.0094 ±0.16	0.1497 ±3.97	0.1238 ±4.01	0.1574 ±3.71
Andradite	0.0243 ±0.13	-	-	-
Buddingtonite	0.0033 ±0.10	0.0958 ±4.69	0.1021 ±3.47	0.1412 ±3.74
Dumortierite	0.0043 ±0.16	-	-	-
Kaolinite-1	0.0249 ±0.13	0.0885 ±2.94	0.0986 ±3.18	0.0736 ±4.42
Kaolinite-2	0.0459 ±0.10	0.1206 ±3.67	0.1375 ±3.48	0.1420 ±4.16
Muscovite	0.0058 ±0.08	0.1024 ±4.24	0.1061 ±3.18	0.1007 ±3.31
Montmorillonite	0.0427 ±0.13	0.0651 ±3.08	0.0705 ±3.36	0.0974 ±3.39
Nontronite	0.0978 ±0.08	0.1138 ±4.15	0.1046 ±3.80	0.0772 ±2.10
Pyrope	0.0044 ±0.15	0.1106 ±3.32	0.1208 ±3.83	0.1437 ±3.76
Sphene	0.0269 ±0.08	0.1024 ±3.79	0.1179 ±4.02	0.1277 ±4.08
Chalcedony	0.0910 ±0.10	0.1496 ±4.12	0.1221 ±4.02	0.1514 ±3.83

Table 5: RMSE results for Cuprite Data (for all the other methods except LDVAE, we have only the average RMSE over all materials, while for LDVAE we have the RMSE results for each material. The results of the other algorithms are collected from Zhang et al. [2021a]).

	LDVAE	SSWNMF	SGSNMF	GLNMF
Alunite	0.0070 ±0.00			
Andradite	0.0050 ±0.02			
Buddingtonite	0.0069 ±0.01			
Dumortierite	0.0070 ±0.00			
Kaolinite-1	0.0120 ±0.06			
Kaolinite-2	0.0069 ±0.00	0.0043 ±0.05	0.0055 ±0.06	0.0040 ±0.06
Muscovite	0.0069 ±0.00			
Montmorillonite	0.0056 ±0.01			
Nontronite	0.0272 ±0.08			
Pyrope	0.0161 ±0.06			
Sphene	0.3603 ±0.22			
Chalcedony	0.0070 ±0.01			

Table 6: SAD results for Hydice Urban dataset (The results of the other algorithms are collected from Zhang et al. [2021a]).

	LDVAE	SSWNMF	SGSNMF	TV-RSNMF	RSNMF	GLNMF	L1/2-NMF	VCA
Asphalt Road	0.6460 ±0.01	0.0782 ±3.29	0.0804 ±4.01	0.0770 ±2.97	0.0869 ±3.81	0.1008 ±3.19	0.0889 ±2.88	0.2246 ±3.00
Grass	0.2708 ±0.11	0.1490 ±3.58	0.1516 ±3.25	0.1495 ±3.54	0.1594 ±3.62	0.1531 ±3.06	0.1452 ±3.57	0.1981 ±3.00
Tree	0.3327 ±0.16	0.1173 ±3.46	0.1199 ±3.36	0.1269 ±4.02	0.1457 ±4.29	0.1424 ±3.79	0.1509 ±3.18	0.2137 ±2.90
Roof	0.4690 ±0.24	0.0713 ±3.61	0.0731 ±3.54	0.0746 ±4.09	0.0849 ±3.90	0.0986 ±4.62	0.0863 ±4.06	0.2673 ±3.00
Metal	0.6509 ±0.07	0.1241 ±2.76	0.1250 ±3.81	0.1247 ±3.53	0.1324 ±4.15	0.1370 ±4.28	0.1334 ±3.90	0.1848 ±3.00
Dirt	1.0268 ±0.63	0.0802 ±3.17	0.0859 ±3.91	0.0849 ±3.92	0.0798 ±3.77	0.1059 ±3.96	0.1063 ±3.54	0.1992 ±3.00

Table 7: RMSE results for Hydice Urban dataset (for all the other methods except LDVAE, we have only the average RMSE over all materials, while for LDVAE we have the RMSE results for each material. The results of the other algorithms are collected from Zhang et al. [2021a]).

	LDVAE	SSWNMF	SGSNMF	L1/2-NMF
Asphalt Road	0.0524 ± 0.08			
Grass	0.0333 ± 0.16			
Tree	0.0301 ± 0.17			
Roof	0.0156 ± 0.07	0.0048 ± 0.72	0.0061 ± 0.67	0.0044 ± 0.76
Metal	0.0078 ± 0.02			
Dirt	0.0178 ± 0.12			

Table 8: SAD results for Samson Data.

LDVAE	
1-soil	0.0877 ± 0.31
2-tree	1.3956 ± 0.30
3-water	0.3260 ± 0.38

micro-spectroscopy where each material has, intrinsically, several elements in its composition. This scenario is also relevant in Remote Sensing and HSI images with low-spatial resolution.

As demonstrated in the Figure 4, the estimation of abundances can be calculated using the Encoder stage of LDVAE. Subsequently, the Decoder stage can generate the signal of pure endmembers with the abundances of a pure pixel being assigned into z . Figure 5 shows how we can feed the Decoder stage of our model with the one-hot vector, as they indicate “pure classes.”

The results show that LDVAE performed satisfactorily in all scenarios, with special attention to the experiments on Cuprite dataset. The results on synthetic data are aggregated over all classes, as we focused on the robustness to the noise. The LDVAE model presented itself very consistent to all noise levels, even though not always the top performer. The results on tables 2 and 3 demonstrate the LDVAE performed similarly to the other methods, however the performance does not degrade when the noise rise to higher levels. We attribute this behavior to the fact that LDVAE learned the small variability on pixel values due to the probabilistic approach of Variation Autoencoders. However, this variability also affected the absolute values of the pixels during reconstruction. In other words, the LDVAE managed to average out the noise, while also explains the smaller capacity of reconstructing the spectra but keeping the efficacy on classification (Table 3). The images in Figure 6 show results of classification results compared to the ground truth.

The table 4 indicates that endmember extraction on Cuprite dataset performed noticeably well, also observed in Figure 9. The experiments on Cuprite dataset were distinct compared to the others datasets due to its lack of ground truth. For this reason, we used the same set of materials to generate a random datacube with random mixes. The model, trained only on the synthetic mixed pixels, showed capable of extracting endmembers with small errors, even though the model has never “seen” the endmembers (i.e., only a set of pixels randomly mixed). The RMSE errors on the table 5 also demonstrate good capacity of endmembers extraction, despite not achieving the top results when compared to the

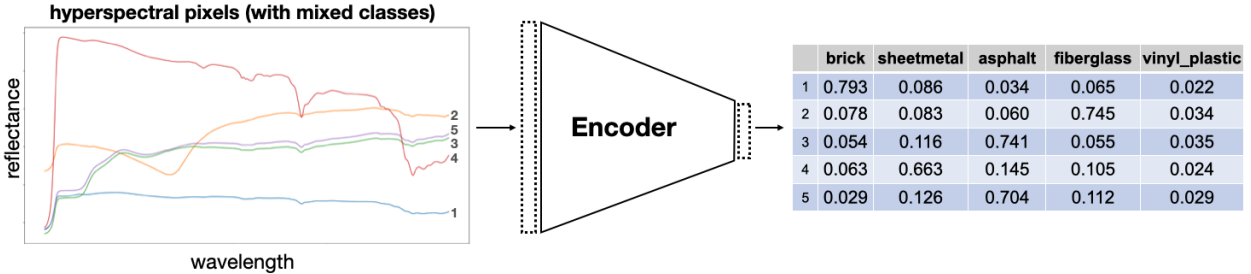


Figure 4: LDVAE-Encoder: pixel classification (or estimation of abundances).

Table 9: RMSE results for Samson Data (for all the other methods except LDVAE, we have only the average RMSE over all materials, while for LDVAE we have the RMSE results for each material. The results of the other algorithms are collected from Borsoi et al. [2019]).

	LDVAE (SAD)	LDVAE (RMSE)	FCLS (RMSE)	PLMM (RMSE)	ELMM (RMSE)	GLMM (RMSE)	DeepGU (RMSE)
soil	0.0877 ± 0.31	0.0678					
tree	1.3956 ± 0.30	0.1196	0.0545	0.0239	0.0119	0.0006	0.0862
water	0.3260 ± 0.38	0.1002					

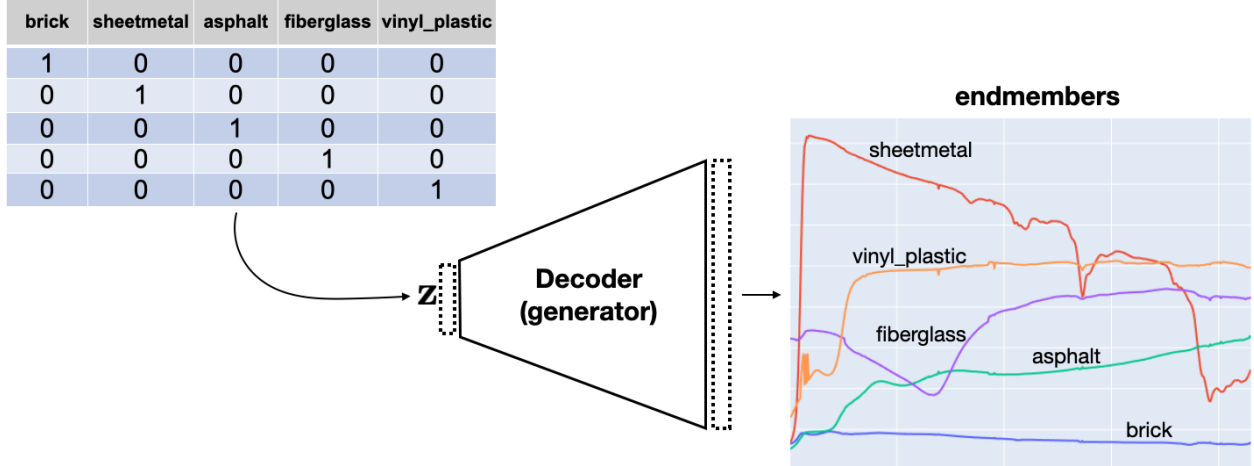


Figure 5: LDVAE-Decoder: extraction (generation) of endmembers from a hot-encoded vector of abundances

state-of-art models. Notice that we have only the average over all materials, except for the LDVAE we have RMSE for each material. Considering the lack of ground truth data to train the model, we consider these results a success, with room for improvements as we will discuss in Section 8.

The worst performance of LDVAE was on the HYDICE Urban dataset, even though it had the larger training set. We used the 50/50 split strategy for training and evaluation of this model. We started with an initial random separation; then, we manually fixed some unbalanced classes. This step should be revisited in the advent of improving performance results on this dataset.

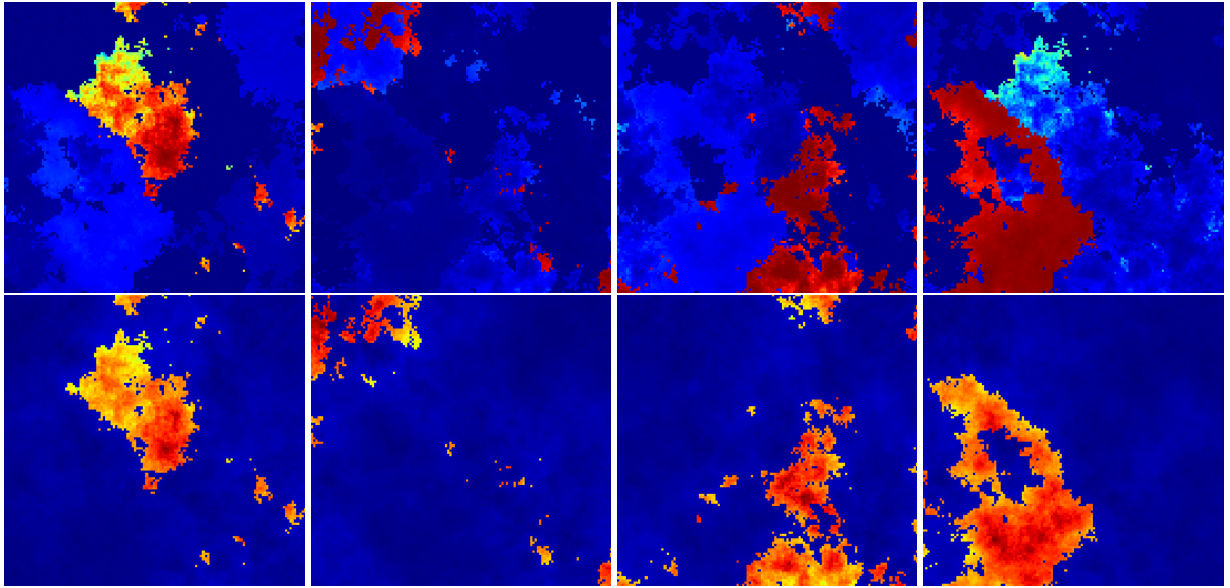


Figure 6: Abundance maps of the synthetic dataset (top row: LDVAE, bottom row: ground truth)

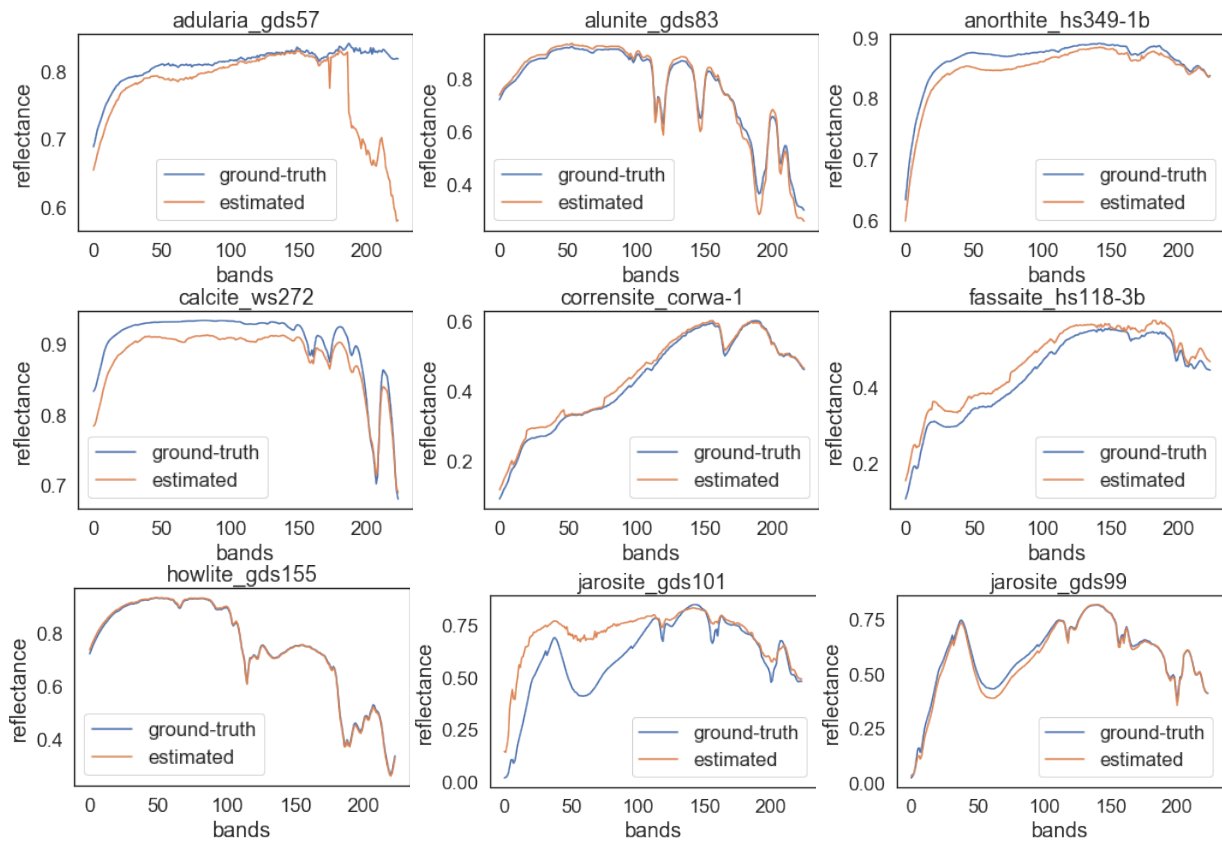


Figure 7: Endmembers of the Synthetic dataset generated by LDVAE: comparison with ground-truth.

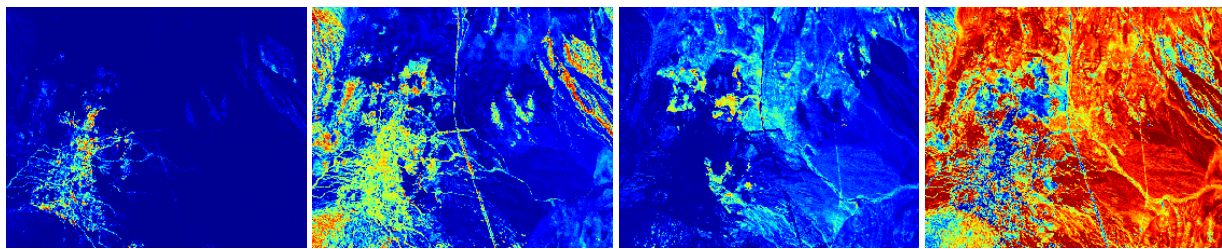


Figure 8: Abundance maps of the Cuprite dataset estimated by LDVAE (ground truth not available). From left to right: Kaolinite1, Nontronite, Pyrope, Sphene

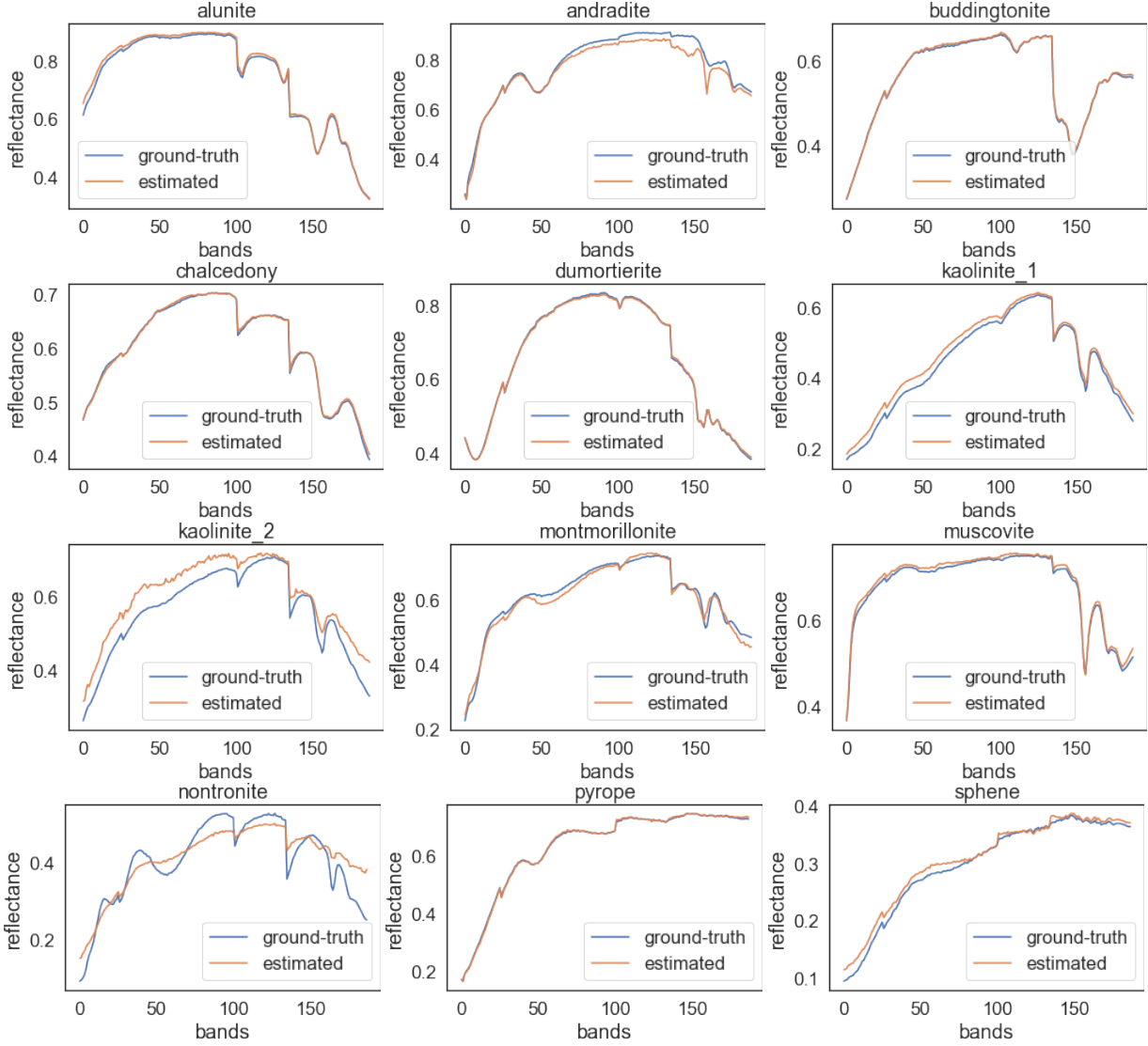


Figure 9: Endmembers of the Cuprite dataset generated by LDVAE: comparison with ground-truth.

The results on Samson dataset were also satisfactory despite the small amount of ground truth data available for training. From Figure 12 we can see that the abundances estimation could detect the prominent classes, but the proportion of material we not properly estimated. Figure 13 shows a moderate performance on endmember extraction, however noisy, in some parts of the spectra (see Figure 13, material=tree, bands 100-150).

8 Conclusions

We present a Latent Dirichlet Variational Autoencoder (LDVAE) model to solve the problem of hyperspectral pixel unmixing. Given a pixel spectra, the proposed model is able to infer endmembers and their mixing ratios together. Furthermore, the proposed model is able to generate spectra of endmembers or of mixed pixels. We evaluate our model on synthetic data constructed from USGS spectra library and on standard benchmarks for hyperspectral pixel unmixing. We have compared our approach with seven commonly used state-of-the-art methods. A drawback of our approach is that it requires labelled data for training; however, we demonstrate that our model can leverage transfer learning. Specifically, we show that it is possible to train the model on synthetic data only and use it subsequently on “real” data. The results suggest that our model is able to match, and sometimes exceed, the performance achieved by the current state-of-the-art method SSWNMF, which assumes *a priori* knowledge of the endmembers present in the pixel to compute abundances.

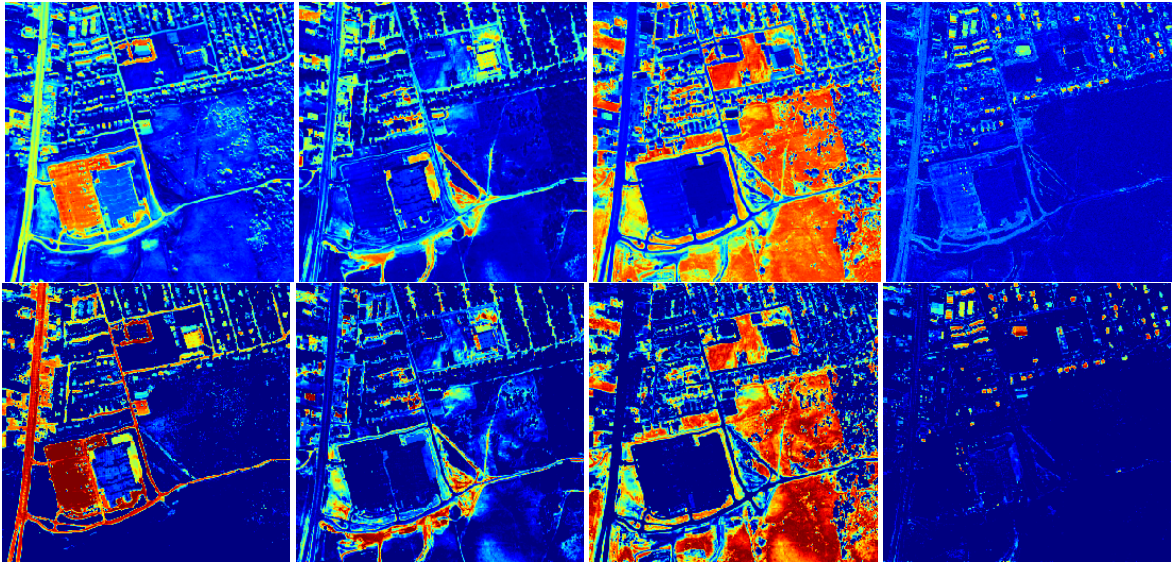


Figure 10: Abundances maps of the HYDICE Urban dataset (top row: LDVAE, bottom row: ground truth). From left to right: asphalt, dirt, grass, metal

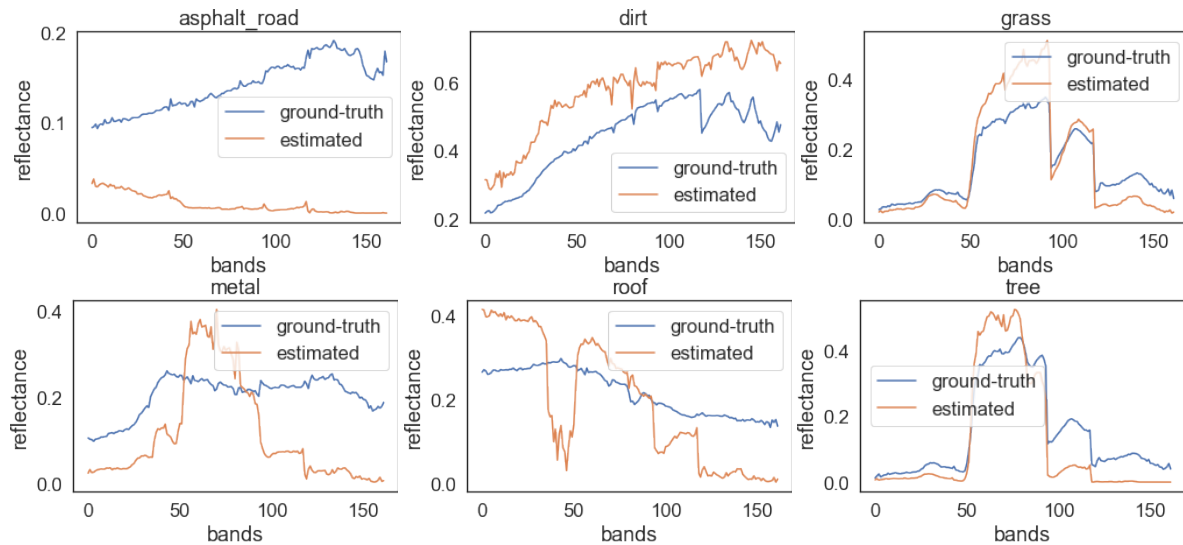


Figure 11: Endmembers of the HYDICE Urban dataset generated by LDVAE: comparison with ground-truth.

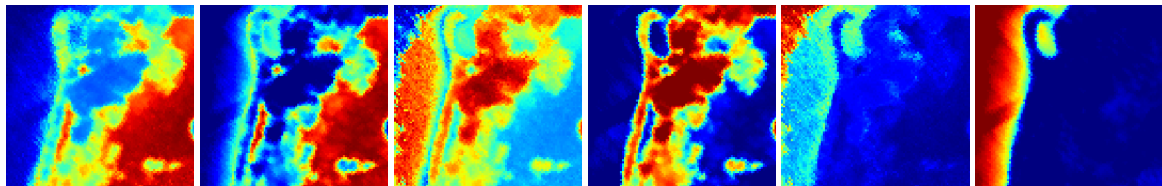


Figure 12: Abundances maps of the Samson dataset (from left to right respectively: Soil, Tree, Water, LDVAE and ground truth are side by side

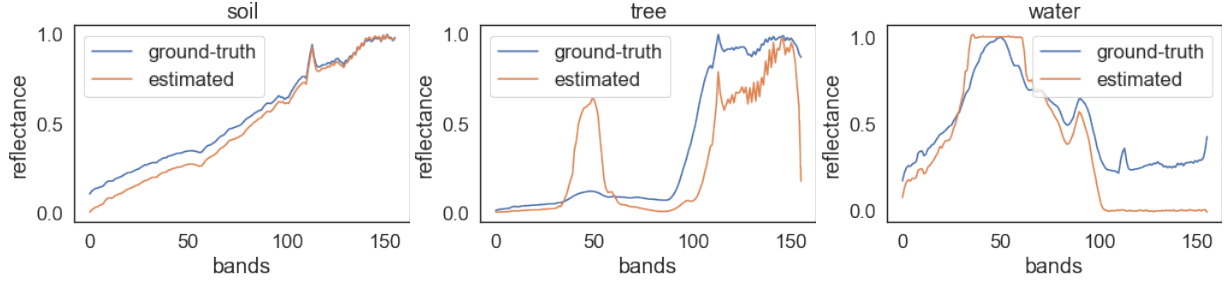


Figure 13: Endmembers of the Samson dataset generated by LDVAE: comparison with ground-truth. From left to right: Soil, Tree and Water. The curves show the estimated and the ground truth endmembers.

In the future, we plan to use spatial information in addition to spectral information for the purposes of pixel unmixing. We also plan to study the feasibility of generating (mixed) pixel spectra for the purposes of hyperspectral image super resolution. Another line of inquiry would be to study how much training data—synthetic or otherwise—is needed to achieve the desired performance.

Acknowledgments

We acknowledge the support of the Natural Sciences and Engineering Research Council of Canada (NSERC) through the NSERC Discovery Program for the funding of the hyperspectral image acquisition mission and image preprocessing facility (RGPIN-386183 awarded to Dr. Yuhong He), and for the Visual Computing Lab of the Ontario Tech University (RGPIN-2020-05159, awarded to Dr. Faisal Z. Qureshi).

References

Rob Heylen, Mario Parente, and Paul Gader. A review of nonlinear hyperspectral unmixing methods. *IEEE Journal of Selected Topics in Applied Earth Observations and Remote Sensing*, 7(6):1844–1868, 2014.

Emmanuel Maggiori, Antonio Plaza, and Yuliya Tarabalka. Models for hyperspectral image analysis: From unmixing to object-based classification. In Gabriele Moser and Josiane Zerubia, editors, *Mathematical Models for Remote Sensing Image Processing: Models and Methods for the Analysis of 2D Satellite and Aerial Images*, pages 37–80. Springer International Publishing, Cham, 2018. ISBN 978-3-319-66330-2. doi:10.1007/978-3-319-66330-2_2.

Shaoquan Zhang, Guorong Zhang, Fan Li, Chengzhi Deng, Shengqian Wang, Antonio Plaza, and Jun Li. Spectral-spatial hyperspectral unmixing using nonnegative matrix factorization. *IEEE Transactions on Geoscience and Remote Sensing*, 2021a.

Urvashi Garg et al. A comprehensive review of hsi in diverse research domains. *Materials Today: Proceedings*, 2021.

Farshid Khajehrayeni and Hassan Ghassemian. A linear hyperspectral unmixing method by means of autoencoder networks. *International Journal of Remote Sensing*, 42(7):2517–2531, 2021.

Min Zhao, Xiuheng Wang, Jie Chen, and Wei Chen. A plug-and-play priors framework for hyperspectral unmixing. *IEEE Transactions on Geoscience and Remote Sensing*, 2021.

Antonio Plaza and Chein-I Chang. Fast implementation of pixel purity index algorithm. In *Algorithms and Technologies for Multispectral, Hyperspectral, and Ultraspectral Imagery XI*, volume 5806, pages 307–317. International Society for Optics and Photonics, 2005.

Javier Plaza, Eligius MT Hendrix, Inmaculada García, Gabriel Martín, and Antonio Plaza. On endmember identification in hyperspectral images without pure pixels: A comparison of algorithms. *Journal of Mathematical Imaging and Vision*, 42(2-3):163–175, 2012.

Diederik P Kingma and Max Welling. Stochastic gradient vb and the variational auto-encoder. In *Second International Conference on Learning Representations, ICLR*, volume 19, page 121, 2014.

U. S. Geological Survey, Raymond F. Kokaly, Roger N. Clark, Gregg A. Swayze, K. Eric Livo, Todd M. Hoefen, Neil C. Pearson, Richard A. Wise, William M. Benzel, Heather A. Lowers, Rhonda L. Driscoll, and Anna J. Klein. Usgs spectral library version 7. Technical report, U. S. Geological Survey, Reston, VA, 2017. URL <http://pubs.er.usgs.gov/publication/ds1035>.

Cuprite dataset. <https://rslab.ut.ac.ir/data> (last accessed on November 16, 2021).

Hydice urban hsi dataset. <https://rslab.ut.ac.ir/data> (last accessed on November 16, 2021).

Samson hsi dataset. <https://rslab.ut.ac.ir/data> (last accessed on November 16, 2021).

Shipeng Zhang, Lizhi Wang, Lei Zhang, and Hua Huang. Learning tensor low-rank prior for hyperspectral image reconstruction. In *Proceedings of the IEEE/CVF Conference on Computer Vision and Pattern Recognition (CVPR)*, pages 12006–12015, June 2021b.

Tao Zhang, Ying Fu, and Cheng Li. Hyperspectral image denoising with realistic data. In *Proceedings of the IEEE/CVF International Conference on Computer Vision (ICCV)*, pages 2248–2257, October 2021c.

Lei Zhang, Jiangtao Nie, Wei Wei, Yanning Zhang, Shengcai Liao, and Ling Shao. Unsupervised adaptation learning for hyperspectral imagery super-resolution. In *Proceedings of the IEEE/CVF Conference on Computer Vision and Pattern Recognition (CVPR)*, June 2020.

Lizhi Wang, Chen Sun, Ying Fu, Min H. Kim, and Hua Huang. Hyperspectral image reconstruction using a deep spatial-spectral prior. In *Proceedings of the IEEE/CVF Conference on Computer Vision and Pattern Recognition (CVPR)*, June 2019.

Ricardo Augusto Borsoi, Tales Imbiriba, and José Carlos Moreira Bermudez. Deep generative endmember modeling: An application to unsupervised spectral unmixing. *IEEE Transactions on Computational Imaging*, 6:374–384, 2019.

Michael E. Winter. N-FINDR: an algorithm for fast autonomous spectral end-member determination in hyperspectral data. In Michael R. Descour and Sylvia S. Shen, editors, *Imaging Spectrometry V*, volume 3753, pages 266 – 275. International Society for Optics and Photonics, SPIE, 1999. doi:10.1117/12.366289. URL <https://doi.org/10.1117/12.366289>.

José M Bioucas-Dias, Antonio Plaza, Nicolas Dobigeon, Mario Parente, Qian Du, Paul Gader, and Jocelyn Chanussot. Hyperspectral unmixing overview: Geometrical, statistical, and sparse regression-based approaches. *IEEE journal of selected topics in applied earth observations and remote sensing*, 5(2):354–379, 2012.

Joseph W Boardman, Fred A Kruse, and Robert O Green. Mapping target signatures via partial unmixing of aviris data. *Proc. Summ. JPL Airborne Earth Sci. Workshop*, 1:23–26, 1995.

Mario Parente and Antonio Plaza. Survey of geometric and statistical unmixing algorithms for hyperspectral images. In *2010 2nd Workshop on Hyperspectral Image and Signal Processing: Evolution in Remote Sensing*, pages 1–4. IEEE, 2010.

P. Ghamisi, N. Yokoya, J. Li, W. Liao, S. Liu, J. Plaza, B. Rasti, and A. Plaza. Advances in hyperspectral image and signal processing: A comprehensive overview of the state of the art. *IEEE Geoscience and Remote Sensing Magazine*, 5(4):37–78, Dec 2017. ISSN 2373-7468. doi:10.1109/MGRS.2017.2762087.

Daniel C Heinz et al. Fully constrained least squares linear spectral mixture analysis method for material quantification in hyperspectral imagery. *IEEE transactions on geoscience and remote sensing*, 39(3):529–545, 2001.

David M. Blei, Andrew Y. Ng, and Michael I. Jordan. Latent dirichlet allocation. *J. Mach. Learn. Res.*, 3:993–1022, March 2003. ISSN 1532-4435. URL <http://dl.acm.org/citation.cfm?id=944919.944937>.

Weonyoung Joo, Wonsung Lee, Sungrae Park, and Il-Chul Moon. Dirichlet variational autoencoder. *Pattern Recognition*, 107:107514, 2020.

Lucas Pinheiro Cinelli, Matheus Araujo Marins, Eduardo Antunio Barros da Silva, and Sergio Lima Netto. *Variational Autoencoder*, pages 111–149. Springer International Publishing, Cham, 2021. ISBN 978-3-030-70679-1. doi:10.1007/978-3-030-70679-1_5. URL https://doi.org/10.1007/978-3-030-70679-1_5.

David M Blei, Alp Kucukelbir, and Jon D McAuliffe. Variational inference: A review for statisticians. *Journal of the American statistical Association*, 112(518):859–877, 2017.

Charles W Fox and Stephen J Roberts. A tutorial on variational bayesian inference. *Artificial intelligence review*, 38(2):85–95, 2012.

Hilda Deborah, Noël Richard, and Jon Yngve Hardeberg. A comprehensive evaluation of spectral distance functions and metrics for hyperspectral image processing. *IEEE Journal of Selected Topics in Applied Earth Observations and Remote Sensing*, 8(6):3224–3234, 2015.

Feiyun Zhu. Hyperspectral unmixing: ground truth labeling, datasets, benchmark performances and survey. *arXiv preprint arXiv:1708.05125*, 2017.

Fan Li, Shaoquan Zhang, Bingkun Liang, Chengzhi Deng, Chenguang Xu, and Shengqian Wang. Hyperspectral sparse unmixing with spectral-spatial low-rank constraint. *IEEE Journal of Selected Topics in Applied Earth Observations and Remote Sensing*, 14:6119–6130, 2021.